The DOI for this manuscript is

DOI:10.2151/jmsj.2019-035

J-STAGE Advance published date: February 4th, 2019

The Development of a Resolution-Independent Tropical Cyclone Detection Scheme for High-Resolution Climate Model Simulations

Akihiko MURATA[1]

Meteorological Research Institute, Tsukuba, Japan

Shun-ichi I. WATANABE

Office of Global Environment and Climate Research Promotion
Japan Meteorological Research Business Support Center, Tsukuba, Japan

Hidetaka SASAKI, Hiroaki KAWASE, and Masaya NOSAKA

Meteorological Research Institute, Tsukuba, Japan

July 26, 2018

---

1) Corresponding author: Akihiko Murata, Meteorological Research Institute, 1-1 Nagamine, Tsukuba, Ibaraki 305-0052, JAPAN.
Email: amurata@mri-jma.go.jp
Tel: +81-29-853-8732
Fax: +81-29-855-7240

Abstract

A novel method for detecting tropical cyclones in high-resolution climate model simulations is proposed herein and subjected to examination. The proposed method utilizes a two-dimensional scatterplot based on two quantities that represent the radial gradient and the tangential asymmetry of mid-to upper-level thickness around a simulated vortex. A comparison between the modeled and observed tropical cyclones using the non-hydrostatic regional climate model (NHRCM) with 20-km grid spacing under reanalysis-driven boundary conditions for one year revealed that no cyclones were missed and there was only one false alarm over a part of the western North Pacific near Japan. The simulated vortices were classified into two categories; tropical cyclones and extratropical cyclones. These two groups, having specific features, were also found in the results using present-day climate datasets, indicating that the tropical cyclones were reasonably distinguished from extratropical cyclones although a one-by-one comparison could not, in principle, be conducted. Comparison of the results obtained from datasets with 5-km and 20-km grid spacing demonstrated that the detection scheme was only weakly dependent on the horizontal resolution. This dependence was further reduced by using the radial gradient over the outer radii instead of near the center of the vortex. The resolution-independent feature in this method is due to a procedure in

which the tangential asymmetry of mid-to upper-level thickness is utilized instead of the relative vorticity at 850 hPa, often used in conventional schemes. This procedure allows the method to identify tropical cyclones without the need to determine a grid-dependent threshold. The method proposed here provides a useful tool for detecting tropical cyclones in high-resolution climate simulations.

Keywords tropical cyclone; detection scheme; tracking; regional climate model

1. Introduction

Based on climate model projections, precipitation extremes will increase in warm climates. According to the fifth assessment report of the United Nations Intergovernmental Panel on Climate Change (IPCC AR5), "extreme precipitation events over most of the mid-latitude land masses and over wet tropical regions will very likely become more intense and more frequent by the end of this century, as the global mean surface temperature increases" (IPCC, 2013). This indicates that the intensity of extreme precipitation, such as the annual daily maximum precipitation, tends to increase more significantly compared with a kind of average precipitation, such as the annual total precipitation and the monthly total precipitation.

An extreme precipitation event is often associated with a tropical cyclone (e.g., Nakano et al. 2010; Kanada et al. 2017). Therefore, examining future changes in the precipitation amounts accompanying tropical cyclones is a crucial issue for estimating changes in precipitation extremes. It is thus necessary to classify precipitation, simulated by climate models, into two categories; precipitation associated with tropical cyclones, and others. To do so, a scheme for detecting tropical cyclones is required. In particular, a scheme suitable for output data from a high-resolution climate model, such as a regional climate model (RCM) and a high-resolution general circulation model (GCM; e.g., Miyamoto et al. 2013), is desirable because our main target is regional precipitation associated with tropical cyclones around Japan in the present and future climates.

77 Many schemes have been proposed for the detection of tropical cyclones in a gridded
78 dataset produced by climate model simulations. Ullrich and Zarzycki (2017) reviewed
79 schemes for tropical cyclone detection (in Appendix B of their paper). They listed many
80 published schemes along with short descriptions. All of the schemes utilized some kind of
81 threshold value to detect tropical cyclones. For example, surface wind speed is often used
82 and a threshold is set to identify tropical cyclones. An appropriate value of the threshold
83 was examined by Walsh et al. (2007) for different horizontal resolutions. They found that
84 the threshold wind speed varied linearly with resolution. It should be noted that the
85 thresholds are sometimes adjusted so that simulated tropical cyclones show a reasonable
86 number (e.g., Oouchi et al. 2006).
87 In many schemes, the 850 hPa relative vorticity near the vortex center needs to exceed a
88 threshold for identifying the vortex as a tropical cyclone. For example, in Bengtsson et al.
89 (1982), one of criteria for identifying tropical cyclones from a forecast model output with
90 about a 200 km resolution was that the 850 hPa relative vorticity maxima were greater than
91 7×10^{-5} s^{-1} in a 7.5° × 7.5° area. Sugi et al. (2002) used an 850 hPa relative vorticity
92 threshold of 7×10^{-5} s^{-1} for a T106 (about 125 km) dataset derived from a GCM. In contrast,
93 the threshold value was 3.5×10^{-5} s^{-1} for a 20 km dataset in Oouchi et al. (2006). On the
94 other hand, Murakami and Sugi (2010) employed resolution dependent thresholds of 850
95 hPa relative vorticity for outputs from GCMs with horizontal resolutions between 20 and 180
96 km. As for RCM datasets, one of the criteria for identifying tropical cyclones from a 60-km

grid RCM dataset in Au-Yeung and Chan (2012) was that the local maximum relative vorticity at 850 hPa was greater than or equal to 4.5×10^{-4} s^{-1}. Huang and Chan (2014) also used this kind of criterion although the threshold value was different.

Temperature anomalies in upper troposphere have also been used to identify tropical cyclones in gridded datasets. This is based on the warm core structure of tropical cyclones. On a practical level, in many schemes, temperature anomalies in upper troposphere near the vortex center need to be larger than a certain threshold. For example, a criterion adopted in Sugi et al. (2002) was that temperature differences from a surrounding area averaged at four pressure levels (i.e., 850, 700, 500, and 300 hPa) was greater than 3 K. Oouchi et al. (2006) and Murakami and Sugi (2010) also used this criterion, but at only three levels (i.e., 700, 500, and 300 hPa); the threshold values were 2 and 1 K, respectively. As for RCM datasets, one of criteria for identifying tropical cyclones used by Au-Yeung and Chan (2012) was that a temperature anomaly at 300 hPa must be 1 K greater than the mean temperature within a 15 degrees radius from the vortex center. Huang and Chan (2014) also utilized the same threshold.

Although many schemes for tropical cyclone detection have been reported, a scheme for climate model datasets with a fine grid length (i.e., a grid spacing from 20 to 5 km) is lacking because these kind of high-resolution datasets have only recently become available. There are several issues to be solved in order to develop a scheme suitable for the high-resolution climate model datasets.

First, thresholds associated with tropical cyclone detection have to be determined for use in the high-resolution datasets because the threshold values depend on the grid resolution. This problem, however, can be avoided when these thresholds are independent of the horizontal resolution. It is therefore desirable to develop a resolution independent scheme for tropical cyclone detection. Recently, Tory et al. (2013a, b) developed a new method that minimized the resolution dependency of the thresholds. One parameter they used was the Okubo–Weiss–Zeta parameter, a large-scale parameter. This method was designed for coarse-resolution datasets. The performance of the scheme was assessed using relatively coarse-resolution datasets (i.e., 1° × 1° grid spacing). It was found that realistic spatio-temporal distributions were detectable using the Okubo–Weiss–Zeta parameter. On the other hand, Satake et al. (2013) developed a new method using a technique called neighbor enclosed area tracking. This technique is based on temporally overlapping areas over a vorticity threshold. In their study, the performance dependence of the proposed scheme on the horizontal resolution of the datasets was examined by comparing the results with 60- and 110-km grid spacings. The results demonstrated that the scheme was relatively independent of the resolution. Although efforts have been undertaken recently, the schemes developed in both of these studies were developed for relatively coarse mesh datasets (i.e. a grid spacing larger than 50 km). It has not been examined whether the previously proposed schemes can be applicable to the finer mesh datasets (i.e., a grid spacing from 20 to 5 km). Schemes for high-resolution datasets are desirable.

Second, using the relative vorticity at 850 hPa is difficult because this level is underground in some mountainous regions in Japan even though this quantity near the vortex center has often been used to detect tropical cyclones in previous schemes. Since the goal of a subsequent study is to investigate future changes in precipitation over Japan associated with tropical cyclones, tropical cyclone tracks over the land in Japan are important.

Third, it is desirable to develop a scheme for cases when the upper-level data are not available due to the limitations of computational and data storage resources. Since the data volumes of RCM and high-resolution GCM datasets are large due to their fine grid spacing and long-term numerical integration, it is possible that only the surface data are provided in order to minimize data storage. Shimura et al. (2017) proposed a tropical cyclone detection method based only on sea level pressure and surface wind speed and found satisfactory performance for their study of extreme wave climates generated by tropical cyclones.

Finally, it is preferable to propose a physically based scheme. The scheme developed in this study is based on the tropical cyclone structure. In particular, the radial gradient and tangential asymmetry were used to extract the tropical cyclones from all the detected vortices. This procedure is similar to a cyclone phase space proposed by Hart (2003). This cyclone phase space was introduced into a scheme for detecting the extratropical transition of tropical cyclones proposed by Zarzycki et al. (2017).

In order to solve these issues, we have proposed a new scheme for detecting tropical

157 cyclones in a gridded dataset produced by high-resolution climate simulations. The goal of
158 this paper is to describe this new scheme and evaluate the detection performance. We
159 show promising results using this scheme. This paper is organized as follows. Section 2
160 describes the data used in this study. Section 3 presents a new scheme for detecting
161 tropical cyclones in output data provided by RCM simulations. This new scheme consists
162 two parts; vortex detection, and tropical cyclone extraction from the detected vortices. In
163 Section 4, the performance of the tropical cyclone detection scheme is evaluated. Three
164 kinds of RCM datasets were used to assess the performance of the scheme. These
165 datasets include a 20-km grid dataset forced by reanalysis data, a 20-km grid dataset
166 forced by an atmospheric general circulation model (AGCM), and a 5-km grid dataset
167 forced by an AGCM. Section 5 discusses several issues related to the performance of the
168 scheme. These issues include the characteristics of identified tropical cyclones. Case
169 studies using only the surface data and using the gradient over the outer radii were also
170 examined. In addition, the influence of vortex tilt on the tropical cyclone detection scheme
171 was evaluated. Finally, the main results of the study are summarized in section 6. A
172 companion paper (Watanabe et al. 2018) evaluates the precipitation associated with
173 tropical cyclones in the present climate simulated by a RCM and will analyze the projected
174 precipitation in a warm climate.
175
176 **2. Data**

177 Three kinds of RCM datasets were employed in order to assess the performance of the
178 new tropical cyclone detection scheme from regional climate model data. All datasets were
179 produced by regional climate simulations using the non-hydrostatic regional climate model
180 (NHRCM; Sasaki et al. 2008) developed by the Meteorological Research Institute (MRI) of
181 the Japan Meteorological Agency (JMA), based on the JMA non-hydrostatic model
182 (JMA-NHM; Saito et al. 2006, 2007). The specification of NHRCM are also described in
183 Nakano et al. (2012) and Murata et al. (2015). Data near the lateral boundaries were not
184 used to minimize their impacts.

185 First, a gridded dataset, with 20-km grid spacing, whose boundary conditions were set
186 from reanalysis data (Nosaka et al. 2014) was used so that detected tropical cyclones in the
187 modeled data could be directly compared with observed tropical cyclones. The model
188 domain covered 18°–47° N and 116°–150° E (Fig. 1). The simulation was started on
189 September 1, 2006 and allowed to run for 1 year. As for the observed data, the best track
190 data provided by the Regional Specialized Meteorological Center (RSMC)-Tokyo were used,
191 except for a part of the extratropical transition. The reanalysis data were produced by the
192 JMA Climate Data Assimilation System (JCDAS), and was the temporally extended version
193 of the Japanese 25-year Reanalysis data (JRA-25; Onogi et al. 2007).

194 Second, a gridded dataset, with 20-km grid spacing that represented the present climate
195 (Kawase et al. 2014; Murata et al. 2016) was used. The model domain covered 18°–47° N
196 and 117°–153° E (Fig. 1). The simulation was started on September 1, 1984 and was

Fig.1

allowed to run for 20 years. The boundary conditions for the simulation were provided by a simulation with an AGCM with a 60-km horizontal resolution (MRI-AGCM3.2H, hereafter referred to as AGCM60; Mizuta et al. 2012).

Third, a gridded dataset with 5-km grid spacing (Murata et al. 2015) was used. Similar to the second dataset, this dataset also represented the present climate. However, the simulation was conducted using a higher horizontal resolution; the grid spacing was 5 km instead of 20 km. The four corners of the model domain were 26° N, 113° E, 15° N, 132° E, 57° N, 140° E, 38° N, and 162° E (Fig. 1). The simulation was started on September 1, 1980 and allowed to run for 20 years. The boundary conditions for the simulation were provided by a simulation with an AGCM with a 20-km horizontal resolution (MRI-AGCM3.2S, hereafter referred to as AGCM20; Mizuta et al. 2012).

3. Tropical cyclone detection method

The procedure for detecting tropical cyclones in the RCM results is divided into two parts; vortex detection and the extraction of tropical cyclones from the detected vortices. The two procedures are described below.

3.1 Vortex detection

First, vortices including tropical cyclones are identified in the RCM results. A vortex is assumed to satisfy all of the following criteria.

1) The local minimum sea level pressure (MSLP) is lower than a certain threshold. In this study, the threshold value was set to 1000 hPa. This local minimum is defined as the vortex center.

2) The maximum surface wind speed, within a square area whose center corresponds to the vortex center, is greater than 17 m s^{-1}. A square 200 km on a side was set in this study. The maximum surface wind speed can be realistically represented in NHRCM because of its higher resolution.

3) There are no other vortices within the area defined above. When vortices exist in the area, the vortex that has the lowest MSLP is selected. This criterion allows the scheme to detect the vortex without the need for a spatial filter.

4) The method of vortex tracking was as follows: after a certain period, when a vortex existed within a square area whose center corresponded to the original vortex center before the period, these two vortices were assumed to be identical. A period of 1 h and a square 120 km on a side were set in this study. Setting the period of 1 h is intended to examine 1-h accumulated precipitation.

5) The consecutive period during which the three criteria above (i.e., the items 1, 2, 3 and 4) are satisfied is longer than or equal to a certain threshold. The threshold was set 12 h in this study.

3.2 Tropical cyclone extraction from the detected vortices

237 Next, the tropical cyclones were extracted from the detected vortices in the RCM results.
238 The criterion for the extraction was based on the layer thickness between the middle and
239 upper troposphere; 500 and 300 hPa were set in this study (hereafter referred to as *D*). In
240 terms of *D*, quantities related to the radial gradient (*G*) and the tangential asymmetry (*A*) of
241 *D* are defined as follows:
242

$$G = \frac{1}{4}\sum_{i=1}^{4}\left(\frac{D_i - D_0}{R}\right). \quad (1)$$

243
244

$$A = \frac{|D_1 - D_2| + |D_2 - D_3| + |D_3 - D_4| + |D_4 - D_1|}{2\pi R}. \quad (2)$$

245
246 *G* represents the radial gradient of *D* between the vortex center and at a radius (*R*) and *A*
247 represents the tangential asymmetry of *D* along the circumference of *R*. In order to reduce
248 the computational cost, values of *D* were included only at five grid points in Eqs. (1) and (2):
249 at the vortex center (D_0), at 0 (D_1), 90 (D_2), 180 (D_3), and 270 (D_4) degrees in the clockwise
250 direction with respect to the Y axis. In this study, *R* was set at 300 km. The indices, *G* and *A*,
251 are temporally averaged over the period of the vortex lifetime. The relationship between *G*
252 and *A* were utilized to extract the tropical cyclones from all the detected vortices. This
253 procedure is graphically shown in Section 4. It should be noted that a scheme for the
254 extratropical transition of a tropical cyclone will be added in a companion paper (Watanabe

et al. 2018).

4. Evaluation of the tropical cyclone detection scheme

In order to assess the performance of the new tropical cyclone detection scheme from regional climate model data, three kinds of RCM datasets as mentioned in Section 2 were utilized. The results of the performance assessment using each dataset are described below.

4.1 The 20-km grid dataset forced by reanalysis data

First, the vortex detection performance was examined. Examples for fall and winter are displayed in Fig. 1. In fall (Fig. 1a), there were two tropical cyclones around Japan; Typhoon Shanshan (2006) and typhoon Yagi (2006). Generally, Shanshan and Yagi were located west and east of Japan, respectively.

Both the Shanshan and Yagi tracks were captured in the 20-km grid model data (Fig. 1a). For Shanshan, its northeastward movement is represented in the simulation although the detected vortex appeared later and disappeared earlier than in the observations. Similarly, the detected track of Yagi corresponded to observations except for the southern and northern parts; in these parts, an outer region of a tropical cyclone (i.e., R is greater than 300 km) is outside the model domain. Since all vortices were detected, vortices other than tropical cyclones were also included in Fig. 1a. Vortices other than tropical cyclones were

also detected in winter. In Fig. 1b, two vortices were detected around Japan, whereas there were no observed tropical cyclones. This result indicates a requirement for the extraction of tropical cyclones from all simulated vortices.

Next, tropical cyclones were distinguished from other vortices by the relationship between the two indices mentioned above; *G* and *A*. The scatterplot of *A* versus *G* is shown in Fig. 2. It should be noted that these two indices are temporally averaged over the period of the vortex lifetime. A simulated vortex was judged to be a tropical cyclone when the distance between the vortex and an observed tropical cyclone, averaged over the lifetime of the vortex, was within 500 km. The scatterplot revealed that data for the tropical cyclones were located around the lower left of Fig. 2, compared with vortices other than tropical cyclones. That is, the magnitude of *G* for tropical cyclones is greater than for the other vortices (*G* is generally negative); *A* for tropical cyclones is smaller than for the other vortices. This result reflects the warm core structure of tropical cyclones. A warm core, typically located in the middle to upper troposphere, has a structure of negative *G* because the layer between thicknesses of 500 and 300 hPa is thicker near the vortex center than the outer radii. The other index, *A*, has an approximate value of zero because of the axisymmetric structure of tropical cyclones. In contrast, vortices other than tropical cyclones, mainly extratropical cyclones, have neither a warm core structure nor an axisymmetric structure. A line that differentiates the two categories is shown in Fig. 2. The slantwise line was intended to divide subtropical lows (e.g., Ogura et al. 2005, 2009), located a region of

Fig.2

small magnitudes of G and A, into the tropical and extratropical cyclones on the basis of their structure. The equation of the line is as follows:

$$\frac{A}{G} = -\frac{14}{25} = -0.56\,. \tag{3}$$

The left-hand side of Eq. (3) represents an asymmetry index normalized by *G*. The magnitude of *A* is about half the magnitude of *G* in this case although the specific value (i.e., -0.56) is rather arbitrary. This value may depend on climate models.

The results demonstrate that the simulated tropical cyclones were proficiently detected, considering that there were none missed and only one false alarm. This falsely alarmed system was located a subtropical area and did not have a surface front, thereby leading to the judgment that the system was in the tropical cyclone category.

4.2 The 20-km grid dataset forced by the AGCM60

Tropical cyclones were detectable in the 20-km grid RCM dataset, whose boundary conditions were AGCM60 results, by using the criteria mentioned above. The relationship between *G* and *A* seemed to hold true for this dataset (Fig. 3a). The plotted points could be classified into two categories. In the first category, the magnitude of *G* (generally negative) was relatively large and *A* was near zero. In contrast, in the second category, the magnitude of *G* was near zero and *A* was relatively large. The first and second category

Fig.3

corresponded to tropical cyclones and extratropical cyclones, respectively. Result verifications were not performed due to the limits of the present climate simulation data, in which a simulated tropical cyclone does not correspond one-to-one with the observed cyclone. The range of *G* was wider than in the reanalysis forced RCM data (Fig. 2). The maximum magnitude of *G* almost reached 2.5×10^6 m m^{-1} in Fig. 3a, whereas it was below 1.5×10^6 m m^{-1} in Fig. 2. This is probably due to a difference in period data cover that was 20 years in Fig. 3a, and 1 year in Fig. 2. An intensified tropical cyclone that has a large magnitude of *G* can be simulated in a long-term climate experiment, such as in Fig. 3a.

4.3 The 5-km grid dataset forced by the AGCM20

Similar to the 20-km grid datasets, tropical cyclones were detectable in the 5-km grid RCM dataset, whose boundary conditions were the AGCM20 results, by using the criteria described above. The relationship between *G* and *A* seemed to also hold true for this dataset (Fig. 3b). Similarly, there were two categories identified as shown in Fig. 3b. The data in one category had greater magnitudes of *G* and near-zero values for *A*, whereas those in the other category had near-zero *G* and greater *A values*. The former and latter categories corresponded to tropical cyclones and extratropical cyclones, respectively.

The *A* index was less dependent on the horizontal resolution compared to the *G* index. The range of *A* in the 5-km grid dataset (Fig. 3b) was similar to the 20-km grid dataset (Fig. 3a). The maxima of *A* for both were below 3.0×10^6 m m^{-1} (Figs. 3a, b). In contrast, the

range of G in the former dataset was wider than in the latter. The maximum of the magnitude of G exceeds 4.0×10^6 m m^{-1} in Fig. 3b, whereas it was below 2.5×10^6 m m^{-1} in Fig. 3a.

In terms of tropical cyclones, the weak dependence of A on the horizontal resolution is attributed to an adequate representation of the outer radius of a tropical cyclone in both the 20-km and 5-km grid datasets. For proper representation near the vortex center on the other hand, the 20-km grid spacing was insufficient for a tropical cyclone. This is because there is a steep temperature gradient, and hence thickness, near the vortex center. To resolve this fine structure, a finer grid spacing (e.g., 5 km) is required. For this reason, the range of G in the 5-km grid datasets was different from the 20-km grid dataset.

From a practical point of view, a threshold to distinguish between tropical and extratropical cyclones needs to be determined. Specifically, the most favorable line that differentiates the two categories in Figs. 3a, b, similar to that in Fig. 2, should be determined so that the number of identified tropical cyclones becomes nearly equal to the observed climate data. This issue will be discussed in detail in a companion paper (Watanabe et al. 2018).

5. Discussion

5.1 Comparison with Hart (2003)

The relationship between the radial gradient and the outer asymmetry of mid- to upper-

354 tropospheric thicknesses for tropical cyclones has been clarified. The former and latter
355 quantities are represented by the *G* and *A* indices, respectively. In Fig. 3b, the magnitude
356 range of *G* is wider than *A* for the identified tropical cyclones. This means that the degree of
357 the thickness asymmetry at the outer radius is less dependent on the intensity of a tropical
358 cyclones compared with the radial gradient of the thickness. It should be noted that an
359 intensified tropical cyclone tends to have a large magnitude of *G*.

360 Scatter diagrams of the relationship between *G* and *A* (Figs. 3a, b) are similar to a
361 cyclone phase space proposed by Hart (2003). This cyclone phase space was designed to
362 identify the tropical cyclone phases, namely for tropical, extratropical, and hybrid cyclones.
363 The parameters used in this cyclone phase space are the vertical derivative of the
364 horizontal height gradient and the thickness asymmetry. The former parameter that
365 corresponds to *G* in the present study, distinguishes the warm core structure from the cold
366 core structure although the thermal wind relationship is used instead of the direct
367 calculation of the radial gradient. On the other hand, the latter parameter equivalent to *A* in
368 the present study, discriminates between the frontal and non-frontal phase. The cyclone
369 phase space therefore is different from the scatter diagram in the present study although
370 the underlying theories are the same. In addition, the cyclone phase space classifies a
371 vortex into categories at a specific time point, whereas *G* and *A* in the present study are
372 temporally averaged over the vortex lifetime.

373

374 *5.2 A case using only the surface data*

375 Using only the surface data, tropical cyclones can be detected even when the upper data
376 unavailable, although the accuracy is slightly decreased. In these cases, sea level pressure
377 is used instead of the thickness between 500 and 300 hPa in the scatter diagrams for the
378 relationship between *G* and *A*. Figure 4a is a similar diagram to Fig. 2, but uses sea level
379 pressure data. Similar to Fig. 2, there are two groups of data representing tropical and
380 extratropical cyclones. The data for one group, however, mixes with the other group. The
381 mixture of the two categorized data is also found in the 5-km grid dataset although the
382 range of *G* is relatively wide (Fig. 4b). These results can decrease the skill the model for
383 detecting tropical cyclones. Nevertheless, this detection method has the possibility of
384 detecting tropical cyclones even when only the surface data is available, which is not
385 necessarily uncommon for a huge dataset related to the high-resolution climate
386 simulations.

387 The relatively low skill in detecting tropical cyclones using only the surface data is
388 attributable to the structure of tropical and extratropical cyclones at the surface. Intensified
389 extratropical cyclones can have a large magnitude of *G* and a small *A*, similar to those for
390 tropical cyclones, leading to a mixture of the data for tropical and extratropical cyclones in
391 some graph regions. In contrast, the data mixing appears less frequently when using the
392 upper-level data because of the warm core structure that leads to a large magnitude of *G*
393 and a small *A* that does not usually occur in extratropical cyclones.

Fig.4

394

395 *5.3 A case using the gradient over the outer radii*

396 The resolution dependence of the detection method can be improved by substituting
397 radial gradients over the outer radii for those data points near the vortex center. The range
398 of the magnitude of *G* varies with the horizontal resolution as described above (Figs. 3a, b).
399 This dependence on resolution can be reduced when the thickness at the outer radii is
400 used. For example, Figs. 5a, b are the same type of diagrams as Figs. 3a, b, respectively,
401 but use the radial gradient between 300 – 400 km instead of between 0 – 300 km. In Fig. 5,
402 the maximum magnitude of *G* is about 2.0×10^6 m m^{-1} for both the 20- and 5-km grid
403 datasets, indicating that *G* was nearly independent of the horizontal resolution. It is possible,
404 however, that the distinction between tropical and extratropical cyclones is insufficient,
405 particularly in the graph region where both *G* and *A* are nearly zero. In this graph region, the
406 mixture of data for tropical and extratropical cyclones can occur. This is because the
407 differences in *G* over the outer radii between tropical and extratropical cyclones is smaller
408 than near the vortex center. Further study is needed to utilize the radial gradient of the
409 thickness over the outer radii of a tropical cyclone.

Fig.5

410

411 *5.4 Influence of vortex tilt*

412 An issue associated with vortex tilt is addressed here. Several tropical cyclones show
413 that the axes of their vortex center tilt with height due to vertical wind shear. In order to seek

414 the simplest possible detection method, this effect was not considered for the detection of
415 tropical cyclones described above. That is, the vortex center at the upper level is assumed
416 to coincide with the surface for simplicity. In order to examine the effects of vortex tilt on the
417 performance of the tropical cyclone detection, a sensitivity test including this effect was
418 conducted. In this test, the vortex center at an upper level was independently determined.
419 Specifically, the vortex center at 500 hPa was defined as the local minimum of the
420 geopotential height, where the horizontal distance between this minimum and the original
421 were nearest within a square area. A square 100 km on a side area was set in this study.
422 Using the vortex center at 500 hPa, the thickness between 500 – 300 hPa was calculated.
423 When there was no local minimum of the geopotential height at 500 hPa, a no tilt
424 assumption was made.

425 The tropical cyclone detection methods in this study were essentially unaffected by the
426 vortex tilt of the tropical cyclones. This contention is supported by the sensitivity test
427 mentioned above. Figure 6 is the same type of diagram as Fig. 3b, but includes the vortex
428 tilt effect. Comparing Fig. 6 to Fig. 3b reveals that the data distributions in both figures are
429 nearly identical, indicating that the former is able to capture the essential structure of
430 tropical cyclones. One possibility for this result is that *G* and *A* are temporally averaged
431 over the vortex lifetime, and this can reduce the effects of vortex tilt.

Fig.6

432

433 *5.5 Cluster analysis*

A cluster analysis was performed on the three datasets mentioned above in order to find indirect evidence that the presented tropical cyclone detection scheme is reasonable. The cluster analysis used in this study is an agglomerative method, a kind of hierarchical clustering (Wilks 2011). The distance measurement used here is called the cosine distance. A distance between two clusters is defined as the mean distance between all pairs of data in the two clusters (called the 'average linkage').

The cluster analysis suggested that the scheme proposed in this study is skillful enough to detect tropical cyclones. Figures 7a, b, c are the same type of diagrams as Figs. 2, 3a, b, respectively, but use the cluster analysis instead of the presented detection method. Fig.7 Comparing Fig. 7a to Fig. 2 reveals that a group of data in Fig. 7a (open circles) corresponds to the category of tropical cyclones found in Fig. 2 (open circles) and the other group in Fig. 7a (filled diamonds) corresponds to the extratropical cyclones found in Fig. 2 (filled diamonds). More specifically, the threshold line in Fig. 2 can also be applied in Fig. 7a. This nearly equal classification result provides indirect evidence suggesting the rationality of the presented detection scheme. In addition, comparing Fig. 7b, c to Fig. 7a reveals that the classification results in Fig. 7b, c are similar to Fig. 7a. This result suggests that the threshold for dividing the two categories does not vary significantly with the horizontal resolution.

6. Summary and concluding remarks

A new scheme for detecting tropical cyclones in a gridded dataset was developed. The aim was to use high resolution climate model datasets, namely with grid spacings of 20 and 5 km, with a variety of horizontal resolutions and with no change in the thresholds of the scheme. This scheme contains several characteristic features. One of them is that the scheme does not utilize the relative vorticity at 850 hPa that has often been used in other schemes because determining a threshold for identifying tropical cyclones is dependent on the horizontal resolution and importantly, 850 hPa is underground in some mountainous regions, such as central Japan. The latter reason is also important considering that our main target in a companion paper (Watanabe et al. 2018) is the precipitation over mountainous areas of Japan associated with tropical cyclones. Another feature of this scheme is the possibility of detecting tropical cyclones using only the surface data when upper-level data are not available. Note that an extratropical cyclones with small asymmetry can be wrongly judged to a tropical cyclone using only the surface data. Moreover, the classification method used for extracting vortices related to tropical cyclones and extratropical cyclones, is based on a physically plausible technique, similar to the phase space proposed by Hart (2003). In our scatterplots, the radial gradient and the tangential asymmetry of the layer thickness between levels at the middle and upper troposphere were used.

The performance of the tropical cyclone detection scheme was evaluated using three kinds of RCM datasets, a 20-km grid dataset forced by reanalysis data, a 20-km grid

dataset forced by an AGCM, and a 5-km grid dataset forced by an AGCM. Using the first dataset allowed us to compare the detected tropical cyclones with actual observations. The second dataset had the same horizontal resolution as the first but represented the present climate. In this case, comparison between the simulated and observed tropical cyclones should be made statistically because comparing a detected tropical cyclone with an observed cyclone individually is meaningless. The third dataset also used the present climate dataset but at a higher resolution.

Evaluation of the three datasets demonstrated that the scheme proposed in this study can skillfully detect tropical cyclones. In the first dataset, a one-by-one comparison between the simulated and observed tropical cyclones showed that none were missed and there was only one false alarm. The simulated data were classified into two categories; tropical cyclone and extratropical cyclones. The former data group have a greater radial gradient and less tangential asymmetry in terms of layer thickness between 500 and 300 hPa. In contrast, in the latter data group, the gradient is relatively low, and the degree of asymmetry is higher. Simulated tropical cyclones were also detectable in the second and third datasets. For both datasets, the data could be classified into the two groups similar to those for the first dataset, indicating that the scheme has the ability to categorize simulated vortices into tropical and extratropical cyclones.

The categorized data reflects the characteristics of the detected tropical and extratropical cyclones. The relationship between the radial gradient and the tangential asymmetry of the

mid- to upper- tropospheric thickness for tropical cyclones has been clarified. It was found that the degree of the tangential asymmetry of the thickness at the outer radius is less dependent on the intensity of a tropical cyclone compared with the radial gradient of the thickness.

The skillful detection of tropical cyclones using the developed scheme is supported indirectly by a cluster analysis. The result obtained from the cluster analysis was nearly equal to results obtained from the method used in the presented scheme. That is, the simulated data were categorized into two groups; tropical and extratropical cyclones. It was also found that the threshold for dividing the two groups does not vary significantly with the horizontal resolution.

The detection scheme developed in this study is only weakly dependent on the horizontal resolution of a dataset. This weak dependence is attributed to one parameter in the two-dimensional scatter diagram. This parameter is the tangential asymmetry of the layer thickness between 500 and 300 hPa at the outer radii that is not strongly influenced by horizontal resolution. As for the other parameter, the radial gradient of the thickness, it was found that using the quantity over the outer radii instead of near the vortex center has the potential for developing a resolution independent detection method.

Several issues relevant to the performance of the tropical cyclone detection scheme were discussed. One of them is associated with the vortex tilt of tropical cyclones. A sensitivity test revealed that the detection of tropical cyclones in this study was essentially

unaffected by the vortex tilt. Another issue is associated with data availability. Even when only surface data is available, as is often the case with high-resolution climate datasets, the scheme can reliably detect tropical cyclones although the detection skill does not exceed that when the upper data are used.

Our main research target was to analyze the projected precipitation over Japan associated with tropical cyclones using high-resolution simulation results as mentioned above. A companion paper (Watanabe et al. 2018) evaluates the precipitation accompanying tropical cyclones in the present climate and analyzes the projected precipitation in a warm climate.

Acknowledgments

This research was supported by JSPS KAKENHI under Grant Number JP16K00526. A portion of the data was supplied by the SOUSEI and TOUGOU programs of the Ministry of Education, Culture, Sports, Science, and Technology (MEXT) of Japan. Another portion of the datasets used for this study was provided from the Japanese 25-year Reanalysis (JRA-25), the cooperative research project carried out by the Japan Meteorological Agency (JMA), and the Central Research Institute of Electric Power Industry (CRIEPI).

References

534

535 Au-Yeung, A. Y. M., and J. C. L. Chan, 2012: Potential use of a regional climate model in
536 seasonal tropical cyclone activity predictions in the western North Pacific. *Clim. Dyn.*, **39**,
537 783–794.

538 Bengtsson, L., H. Böttger, and M. Kanamitsu, 1982: Simulation of hurricane type vortices in
539 a general circulation model. *Tellus*, **34**, 440–457.

540 Hart, R. E., 2003: A cyclone phase space derived from thermal wind and thermal
541 asymmetry. *Mon. Wea. Rev.*, **131**, 585–616.

542 Huang, W.-R., and J. C. L. Chan, 2014: Dynamical downscaling forecasts of Western North
543 Pacific tropical cyclone genesis and landfall. *Clim. Dyn.*, **42**, 2227–2237.

544 IPCC, 2013: *Climate Change 2013: The Physical Science Basis. Contribution of Working*
545 *Group I to the Fifth Assessment Report of the Intergovernmental Panel on Climate*
546 *Change.* T. F. Stocker, D. Qin, G.-K. Plattner, M. Tignor, S.K. Allen, J. Boschung, A.
547 Nauels, Y. Xia, V. Bex, and P.M. Midgley, Eds., Cambridge University Press, Cambridge,
548 United Kingdom and New York, NY, USA, 1535 pp.

549 Kanada, S., K. Tsuboki, H. Aiki, S. Tsujino, and I. Takayabu, 2017: Future enhancement of
550 heavy rainfall events associated with a typhoon in the midlatitude regions. *SOLA*, **13**,
551 246–251.

552 Kawase, H., H. Sasaki, A. Murata, M. Nosaka, and N. N. Ishizaki, 2014: Future changes in
553 winter precipitation around Japan projected by ensemble experiments using NHRCM. *J.*

554 *Meteor. Soc. Japan*, **92**, 571–580.
555 Miyamoto, Y., Y. Kajikawa, R. Yoshida, T. Yamaura, H. Yashiro, and H. Tomita, 2013: Deep
556 moist atmospheric convection in a subkilometer global simulation. *Geophys. Res. Lett.*,
557 **40**, 4922–4926.
558 Mizuta, R., H. Yoshimura, H. Murakami, M. Matsueda, H. Endo, T. Ose, K. Kamiguchi, M.
559 Hosaka, M. Sugi, S. Yukimoto, S. Kusunoki, and A. Kitoh, 2012: Climate simulations
560 using the improved MRIAGCM with 20-km grid. *J. Meteor. Soc. Japan*, **90A**, 233−258.
561 Murakami, H., and M. Sugi, 2010: Effect of model resolution on tropical cyclone climate
562 projections. *SOLA*, **6**, 73–76.
563 Murata, A., H. Sasaki, H. Kawase, M. Nosaka, M. Oh'izumi, T. Kato, T. Aoyagi, F. Shido, K.
564 Hibino, S. Kanada, A. Suzuki-Parker, and T. Nagatomo, 2015: Projection of future climate
565 change over Japan in ensemble simulations with a high-resolution regional climate model.
566 *SOLA*, **11**, 90–94.
567 Murata, A., H. Sasaki, H. Kawase, and M. Nosaka, 2016: Identification of key factors in
568 future changes in precipitation extremes over Japan using ensemble simulations. *Hydrol.*
569 *Res. Lett.*, **10**, 126–131.
570 Nakano, M., S. Kanada, and T. Kato, 2010: Statistical analysis of simulated direct and
571 indirect precipitation associated with typhoons around Japan using a cloud-system
572 resolving model. *Hydrol. Res. Lett.*, **4**, 6–10.
573 Nakano, M., T. Kato, S. Hayashi, S. Kanada, Y. Yamada, and K. Kurihara, 2012:

574 Development of a 5-km-mesh cloud-system-resolving regional climate model at the
575 Meteorological Research Institute. *J. Meteor. Soc. Japan*, **90A**, 339–350.
576 Nosaka, M., H. Sasaki, A. Murata, and H. Kawase, 2014: Comparison of bias correction
577 methods in terms of winds simulated by a regional climate model. *Proc. of the Fall*
578 *Conference of Meteor. Soc. of Japan*, 480 (in Japanese).
579 Ogura, Y., H. Niino, R. Kumabe, and S. Nishimura, 2005: Evolution of a typhoon-like
580 subtropical low causing severe weather over the Kanto area on 13 October 2003. *J.*
581 *Meteor. Soc. Japan*, **83**, 531–550.
582 Ogura, Y., R. Kumabe, and S. Nishimura, 2009: Initiation and evolution of a subtropical low
583 observed near the Japan islands. *J. Meteor. Soc. Japan*, **87**, 941–957.
584 Onogi, K., J. Tsutsui, H. Koide, M. Sakamoto, S. Kobayashi, H. Hatsushika, T. Matsumoto,
585 N. Yamazaki, H. Kamahori, K. Takahashi, S. Kadokura, K. Wada, K. Kato, R. Oyama, T.
586 Ose, N. Mannoji, and R. Taira, 2007: The JRA-25 Reanalysis. *J. Meteor. Soc. Japan*, **85**,
587 369–432.
588 Oouchi, K., J. Yoshimura, H. Yoshimura, R. Mizuta, S. Kusunoki, and A. Noda, 2006:
589 Tropical cyclone climatology in a global-warming climate as simulated in a 20 km-mesh
590 global atmospheric model: Frequency and wind intensity analysis. *J. Meteor. Soc. Japan*,
591 **84**, 259–276.
592 Saito, K., T. Fujita, Y. Yamada, J. Ishida, Y. Kumagai, K. Aranami, S. Ohmori, R. Nagasawa,
593 S. Kumagai, C. Muroi, T. Kato, H. Eito, and Y. Yamazaki, 2006: The operational JMA

Nonhydrostatic Mesoscale Model. *Mon. Wea. Rev.*, **134**, 1266–1298.

Saito K, J. Ishida, K. Aranami, T. Hara, T. Segawa, M. Narita, and Y. Honda, 2007: Nonhydrostatic atmospheric models and operational development at JMA. *J. Meteor. Soc. Japan*, **85B**, 271–304.

Sasaki, H., K. Kurihara, I. Takayabu, and T. Uchiyama, 2008: Preliminary experiments of reproducing the present climate using the non-hydrostatic regional climate model. *SOLA*, **4**, 25−28.

Satake, Y., M. Inatsu, M. Mori, and A. Hasegawa, 2013: Tropical cyclone tracking using a neighbor enclosed area tracking algorithm. *Mon. Wea. Rev.*, **141**, 3539–3555.

Shimura, T., N. Mori, and M. A. Hemer, 2017: Projection of tropical cyclone-generated extreme wave climate based on CMIP5 multi-model ensemble in the Western North Pacific. *Clim. Dyn.*, **49**, 1449–1462.

Sugi, M., A. Noda, and N. Sato, 2002: Influence of global warming on tropical cyclone climatology: An experiment with the JMA global model. *J. Meteor. Soc. Japan*, **80**, 249–272.

Tory, K. J., S. S. Chand, R. A. Dare, and J. L. McBride, 2013: The development and assessment of a model-, grid-, and basin-independent tropical cyclone detection scheme. *J. Climate*, **26**, 5493–5507.

Tory, K. J., S. S. Chand, R. A. Dare, and J. L. McBride, 2013: An assessment of a model-, grid-, and basin-independent tropical cyclone detection scheme in selected CMIP3 global

climate models. *J. Climate*, **26**, 5508–5522.

Ullrich, P. A., and C. M. Zarzycki, 2017: TempestExtremes: a framework for scale-insensitive pointwise feature tracking on unstructured grids. *Geosci. Model Dev.* **10**, 1069–1090.

Watanabe, S. I., A. Murata, H. Sasaki, H. Kawase, and M. Nosaka, 2018: Projection of future change of tropical cyclone precipitation over Japan with a high-resolution regional climate model. *J. Meteor. Soc. Japan*, submitted.

Walsh, K. J.E., M. Fiorino, C. W. Landsea, and K. L. McInnes, 2007: Objectively determined resolution-dependent threshold criteria for the detection of tropical cyclones in climate models and reanalyses. *J. Climate*, **20**, 2307–2314.

Wilks, D. S., 2011: *Statistical Methods in the Atmospheric Sciences, third ed.* Academic Press, Oxford, UK, 704 pp.

Zarzycki, C. M., D. R. Thatcher, and C. Jablonowski, 2017: Objective tropical cyclone extratropical transition detection in high-resolution reanalysis and climate model data. *J. Adv. Model. Earth Syst.*, **9**, 130–148.

List of Figures

Fig. 1 Examples of detected vortices in (a) fall (September 1, 2006 to November 30,

2006) and (b) winter (December 1, 2006 to February 28, 2007). The black dots represent the observed tropical cyclones (6-h interval) and the colored dots represent the simulated vortices (1-h interval). The green and yellow dots are for the simulated typhoons Shanshan (2006) and Yagi (2006), respectively. The NHRCM20 domain (reanalysis boundary) is shown in (a) and (b) by the thick solid lines. The NHRCM20 (AGCM60 boundary) and the NHRCM05 (AGCM20 boundary) domains are also shown in (a) by the thick dashed lines and the thin solid lines, respectively.

Fig. 2 The radial gradient, between the center and the 300 km radius, of the thickness between 500 and 300 hPa versus the tangential asymmetry of the thickness at the 300 km radius. The open circles and filled diamonds denote tropical cyclones and others (mainly extratropical cyclones), respectively. The 20-km grid dataset forced by the reanalysis data was used.

Fig. 3 The radial gradient, between the center and the 300 km radius, of the thickness between 500 and 300 hPa versus the tangential asymmetry of the thickness at the 300 km radius. (a) The 20-km grid dataset forced by the AGCM60 and (b) the 5-km grid dataset forced by the AGCM20.

Fig. 4 (a) Same as Fig. 2, but sea level pressure was used instead of the thickness

654 between 500 and 300 hPa. (b) Same as Fig. 3b, but sea level pressure was used instead
655 of the thickness between 500 and 300 hPa.
656
657 Fig. 5 Same as Fig. 3, but the horizontal axis represents the radial gradient between the
658 300 and 400 km radii, instead of between the center and the 300 km radius.
659
660 Fig. 6 Same as Fig. 3b, but including the effects of vortex tilt.
661
662 Fig. 7 (a) Same as Fig. 2, but a cluster analysis was used for classifying data into two
663 groups, denoted by the open circles and filled diamonds. The 20-km grid dataset forced
664 by the reanalysis data was used. (b) Same as Fig. 7a, but the 20-km grid dataset forced
665 by the AGCM60 was used. (c) Same as Fig. 7a, but the 5-km grid dataset forced by the
666 AGCM20 was used.
667
668
669

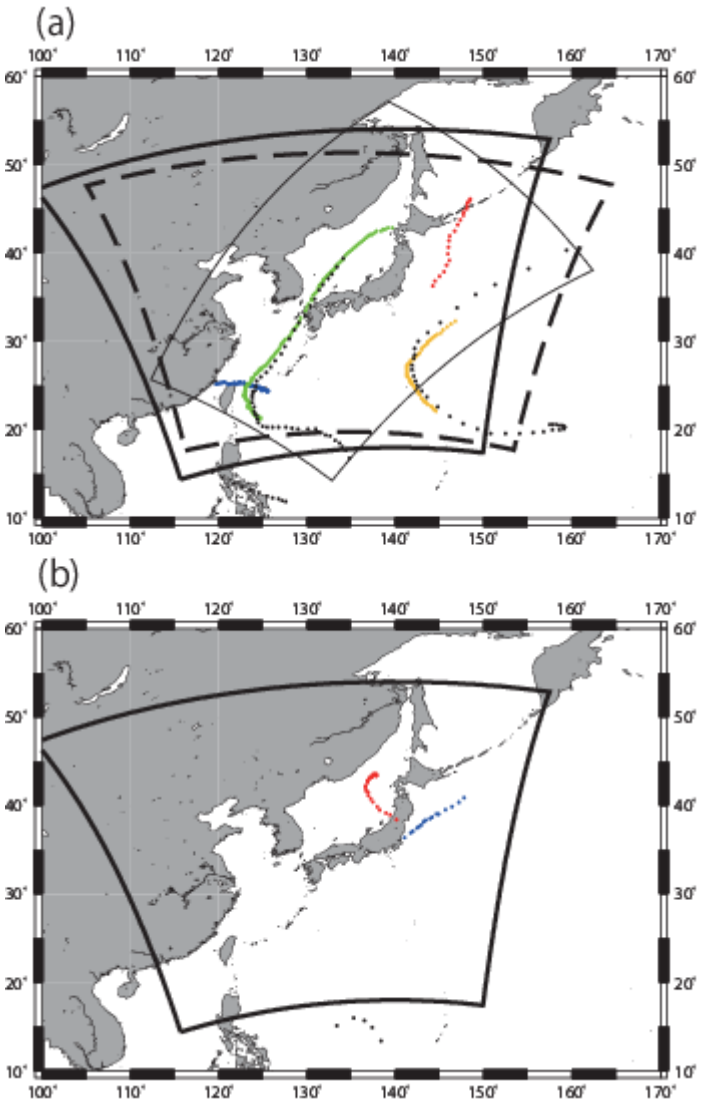

Fig. 1 Examples of detected vortices in (a) fall (September 1, 2006 to November 30, 2006) and (b) winter (December 1, 2006 to February 28, 2007). The black dots represent the observed tropical cyclones (6-h interval) and the colored dots represent the simulated vortices (1-h interval). The green and yellow dots are for the simulated typhoons Shanshan (2006) and Yagi (2006), respectively. The NHRCM20 domain (reanalysis boundary) is shown in (a) and (b) by the thick solid lines. The NHRCM20 (AGCM60

679 boundary) and the NHRCM05 (AGCM20 boundary) domains are also shown in (a) by the

680 thick dashed lines and the thin solid lines, respectively.

681

682

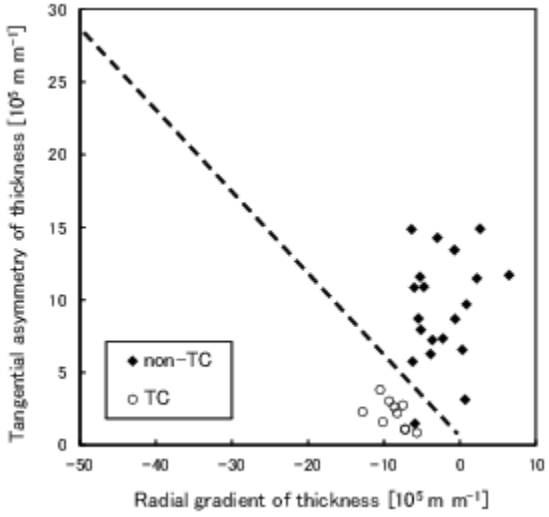

Fig. 2 The radial gradient, between the center and the 300 km radius, of the thickness between 500 and 300 hPa versus the tangential asymmetry of the thickness at the 300 km radius. The open circles and filled diamonds denote tropical cyclones and others (mainly extratropical cyclones), respectively. The 20-km grid dataset forced by the reanalysis data was used.

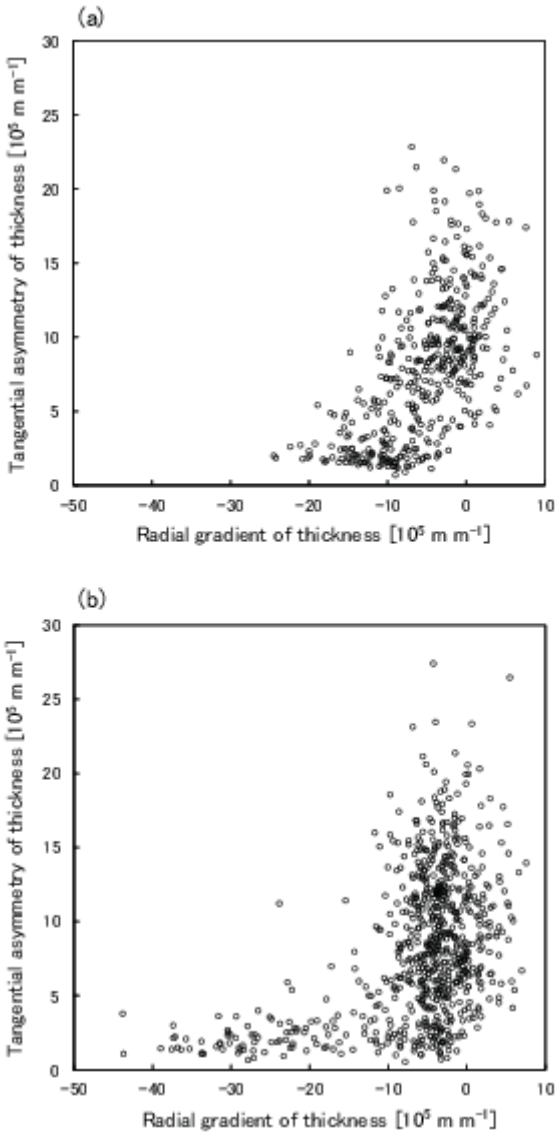

Fig. 3 The radial gradient, between the center and the 300 km radius, of the thickness between 500 and 300 hPa versus the tangential asymmetry of the thickness at the 300 km radius. (a) The 20-km grid dataset forced by the AGCM60 and (b) the 5-km grid dataset forced by the AGCM20.

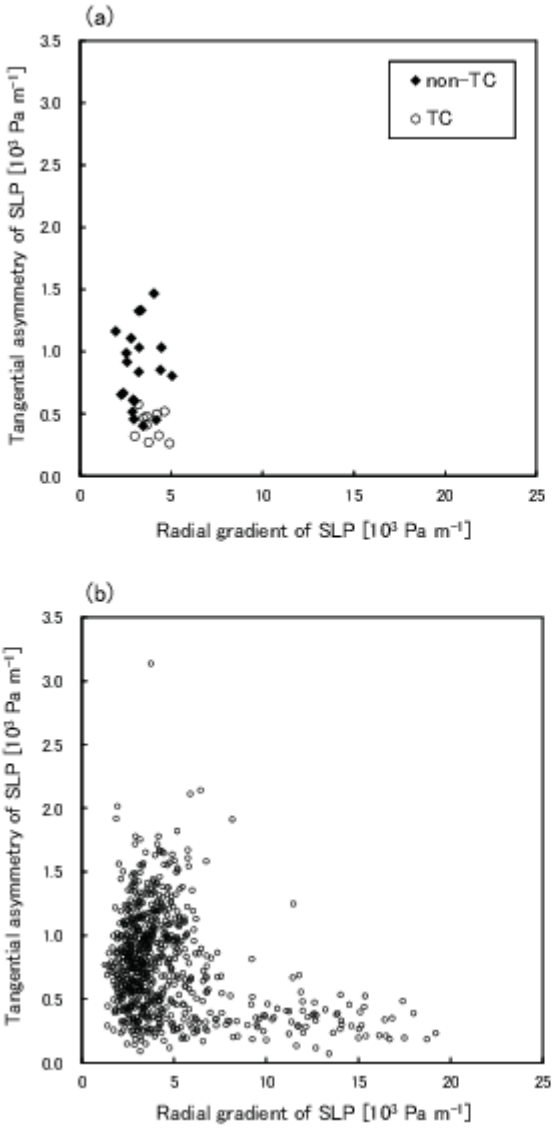

Fig. 4 (a) Same as Fig. 2, but sea level pressure was used instead of the thickness between 500 and 300 hPa. (b) Same as Fig. 3b, but sea level pressure was used instead of the thickness between 500 and 300 hPa.

712

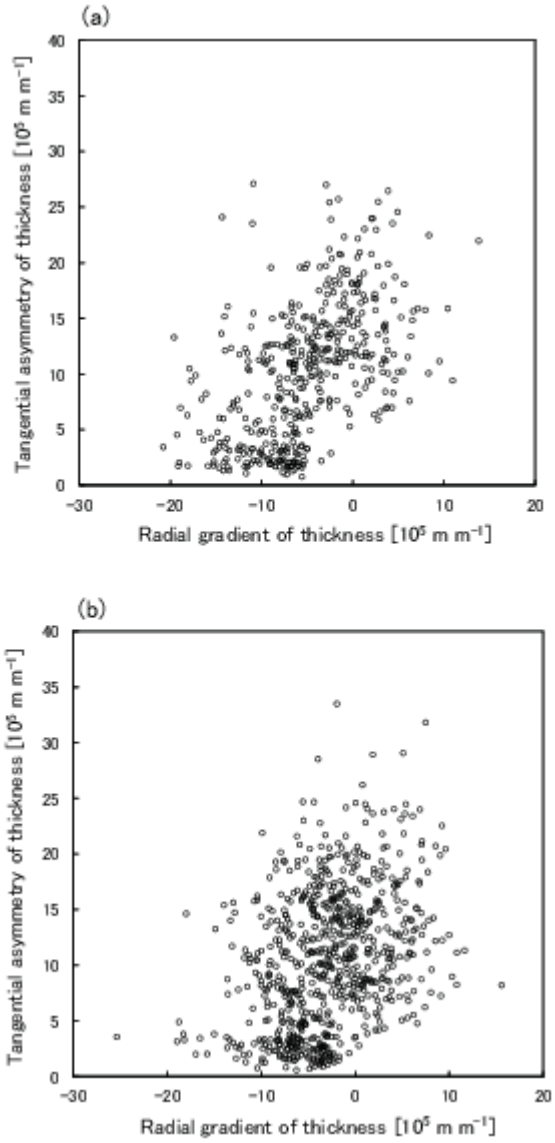

713

714

715 Fig. 5 Same as Fig. 3, but the horizontal axis represents the radial gradient between the

716 300 and 400 km radii, instead of between the center and the 300 km radius.

717

718

719

720

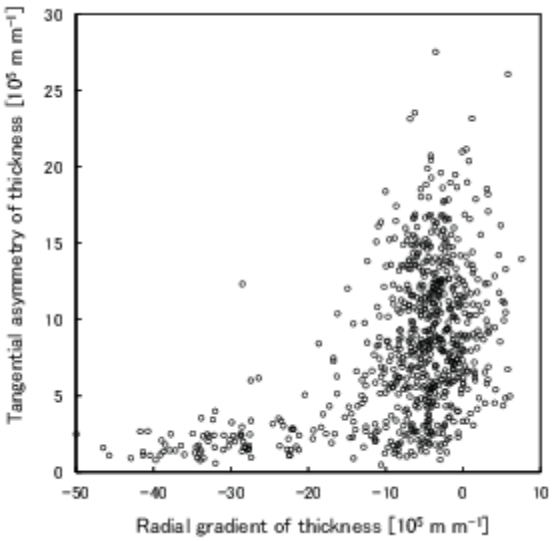

721

722

723 Fig. 6 Same as Fig. 3b, but including the effects of vortex tilt.

724

725

726

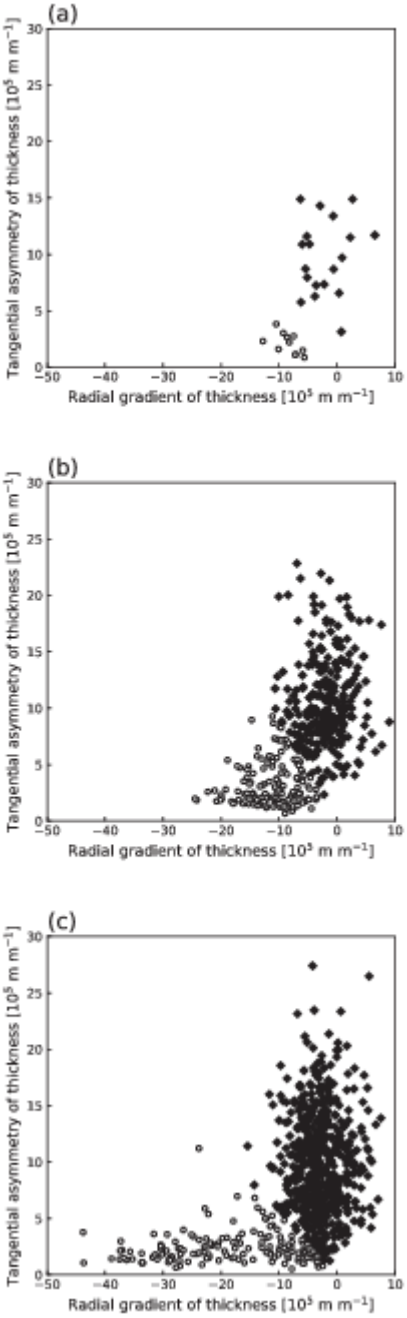

Fig. 7 (a) Same as Fig. 2, but a cluster analysis was used for classifying data into two groups, denoted by the open circles and filled diamonds. The 20-km grid dataset forced by the reanalysis data was used. (b) Same as Fig. 7a, but the 20-km grid dataset forced by the AGCM60 was used. (c) Same as Fig. 7a, but the 5-km grid dataset forced by the

AGCM20 was used.